Sea ice concentration estimation from satellite SAR imagery using convolutional neural network and stochastic fully connected conditional random field

L. Wang A. Wong K. A. Scott D. A. Clausi L.L. Xu M. Shafiee F. Li
System Design Engineering, University of Waterloo
200 University Ave W, Waterloo, ON N2L 3G1
{lei.wang, a28wong, ka3scott, dclausi, l44xu, mjshafiee, f33li }@uwaterloo.ca

Abstract

Ice mapping is important for numerous applications such as ship navigation and mining in the Arctic regions. The need for ice mapping is increasing to support operations in the Arctic regions. We propose an automatic SAR ice concentration estimation method using convolutional neural network (CNN) followed by a stochastic fully connected random field (SFCRF). CNN can generate the proper features for robust ice concentration estimation. The low boundary accuracy of CNN is overcome by introducing SAR image structure information into the CNN output using SFCRF. This method uses ice charts as training data to take advantage of the abundant ice chart archives, which makes it appealing for operational ice mapping purposes. It shows robustness to melting conditions on our test dataset. The overall precision of the ice concentration estimate is less than 0.12 (12%) when validated on ice chart. This method can be naturally extended for ice water classification. An overall classification precision of 96% is achieved by using a simple thresholding on the ice concentration estimates.

1. Introduction

There has been a growing need for accurate high resolution ice maps of the Arctic region in recent years due to increasing human activities in the Arctic region, such as shipping and mining [14, 31]. Monitoring of the sea ice state depends heavily on satellite sensors. Synthetic aperture radar (SAR) is a type of active microwave sensor that is widely used in sea ice mapping [31]. Compared to other types of satellite imaging sensors such as optical and passive microwave sensors, SARs can collect relatively high resolution data (a few meters to one hundred meters) of the earth's surface with or without sun illumination under almost all weather conditions [2]. This is essential for continuous and operational ice monitoring because of the frequent cloud coverage and the long periods with no sun illumination in the Arctic regions.

Due to the lack of robust SAR ice classification and ice concentration estimation algorithms, SAR images are still manually interpreted by ice analysts in ice analysis centers, such as the Canadian Ice Service [4], for operational ice mapping. The manually interpreted ice maps, which are called "ice charts", are composed of large polygons labeled with ice concentration levels (the percentage of ice coverage in the polygon). Ice charts are currently the main data source for operational uses in the Arctic regions.

There has been a constant effort toward automatically ice/water classification and ice concentration estimation in SAR images. Those algorithms normally consist of two steps: feature extraction and classification/regression. Image features such as local backscatter statistics [27, 26, 24, 17, 16, 30, 11, 33], SAR backscatter features [12] and various texture features [23] have been used. Numerous classification/regression models have been used including linear and nonlinear regression [24], neural networks [17, 16], Bayesian classifier [33] and support vector machine [23]. Incorporating spatial context information has also been explored by using image segmentation [30] and MRF models [23].

The effectiveness of classification/regression algorithms using handcrafted features is largely determined by the features used [3]. Robust algorithms require features that can capture the variability of the appearance of ice and water. The difficulty for designing a robust SAR ice concentration estimation algorithm mainly lies in three aspects:

1. Heavy speckle noise contamination of SAR images due to the nature of coherent imaging system [9].

2. Incidence angle effect. The pixels with smaller incidence angles (close to nadir) have larger signal reflectance. Water is more effected compared to ice by the incidence angle effect. Due to the variation of incidence angle, water can appears very dark or even brighter than ice in SAR images.

3. The sensitivity of SAR signals to sea surface conditions such as wind speed, moisture, surface roughness, snow cover and salinity [5]. The appearances of ice and water are very different under different surface conditions (e.g., melting ice and water have similar SAR image appearance).

The complex relationship between SAR signals, the imaging geometry and underlying physical processes makes it challenging to design features for robust ice concentration estimation. A potential solution is to learn image features for the task. This has motivated the use of a convolutional neural network (CNN) as a regression model for ice concentration estimation in this study. CNN has been demonstrated to be able to achieve high performance on complicated image recognition tasks [22, 7, 19, 15] due to its ability to extract robust and abstract representations that are invariant to local image transformations. This invariance also leads to coarser grain of the results. Boundaries and small scale structures are poorly captured which hinders its application in pixel-wise image labeling.

Fully connected conditional random fields (FCRFs) have been proposed to recover details of CNN outputs for semantic labeling [6]. A similar approach is adopted in this work. We build a stochastic fully connected conditional random field (SFCRF) on the CNN output layer to incorporate image structure information to recover detailed structures, especially boundaries. SFCRF is a kind of fully connected CRF, but with randomly selected cliques based on similarity measurement [28]. SFCRF has two major advantages compared to FCRFs [18] in image classification applications: it does not require the pairwise potential function to have certain forms; it can be applied on large images (such as satellite images) efficiently [28].

The training of CNN requires a large amount of training samples to prevent overfitting due to its large number of parameters [19]. Ice charts are used as training samples in the proposed model to take advantage of the abundant archive ice chart available through the Canadian Ice Service. Ice charts are currently produced in ice service centers on a regular basis, so the proposed method can be potentially adopted into operational centers.

There are three main advantages of the proposed method: it is robust to a variety of surface conditions (e.g., during the melting season); it can generate high precision ice concentration with rich details as compared to ice charts; it can be extended for accurate ice/water classification using simple classification algorithm such as thresholding.

2. Methodology

The diagram of the proposed method is illustrated in Fig. 1. The CNN is trained using ice charts, which contain ice concentration at intervals of 10%. The CNN takes dual-band SAR images as input and output ice concentration maps which are then refined by SFCRF. For the purpose of ice water classification, one can apply simple thresholding to the ice concentration maps from CNN-SFCRF.

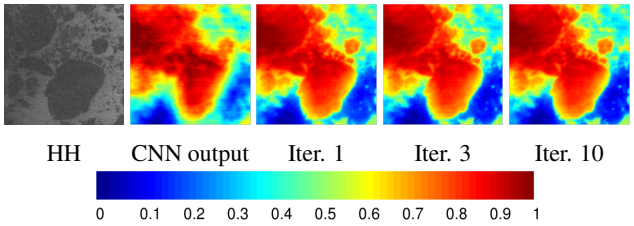

Figure 2: An illustration of SFCRF applied to ice concentration estimate from CNN. The first image is the HH band SAR image in which the dark areas are ice. The second image is the ice concentration estimation from CNN. Image 3 to 5 are the refined ice concentration by SFCRF at iteration 1, 2 and 10 respectively.

2.1. Ice concentration estimation using convolutional neural network

CNN is a type of neural network first proposed by LeCun in 1988 [20] for digits recognition. A CNN is a stack of alternating convolutional layers and pooling layers with one or several fully connected layers on top. The convolutional layers use convolution filters as weights to enforce weight sharing and local connectivity. As a result, the number of weights is decreased compared to fully connected neural networks and spatial information is modeled. A pooling layer is a sub-sampling layer, which is used after each convolutional layer to provide CNN the ability to extract abstract features.

In this study, a three-layer CNN model is used: two convolutional layers in the bottom and one fully connected layer on top. ReLUs (rectified linear unit) are used for convolutional layers and linear units are used for the output layer. The first convolutional layer contains 64 filters of size 7 by 7. The second convolutional layer contains 128 filters of size 5 by 5. The fully connected layer has one unit that generates the ice concentration estimate.

Randomly chosen SAR image patches of size 41 by 41 and the corresponding ice concentration indicated in the ice chart are extracted as training samples. The SAR images used are not always fully covered by the ice charts available, so the number of training samples extracted from each SAR image varies from around 10^3 to 10^4.

Fig. 2 shows an example of estimated ice concentration (column 2). The estimated ice concentration has a blurred appearance. It can capture the existence of ice and water, but boundaries and precise locations of ice are missing. This missing information is recovered by SFCRF. Column 3-5 of Fig. 2 will be described in the next section.

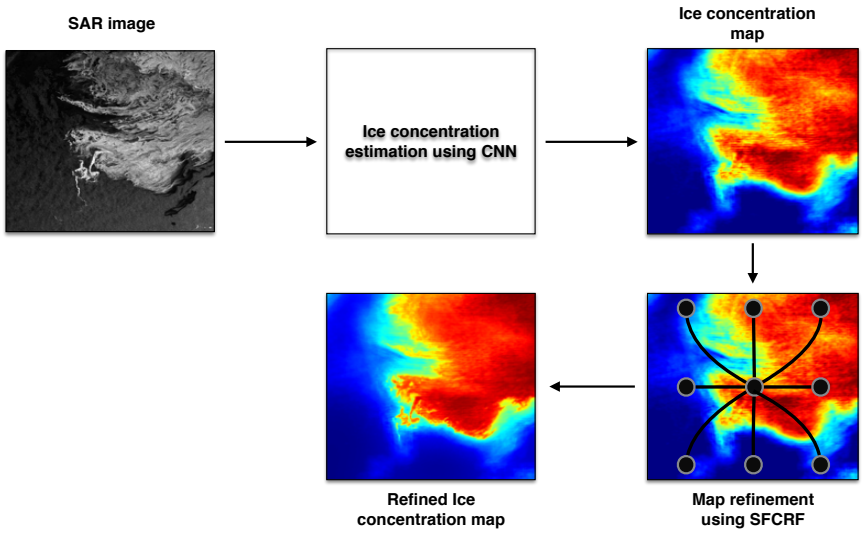

Figure 1: Illustration of the proposed method

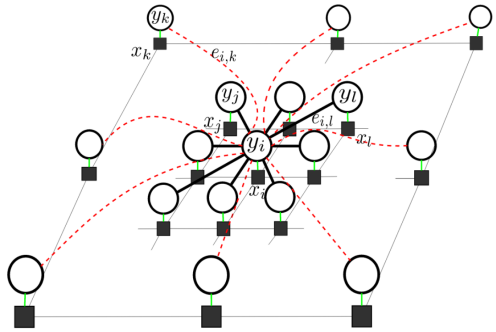

Figure 3: Illustration of SFCRF graph connections. Remote connections (dashed lines) are build in a random manner [28].

2.2. Ice concentration map refinement using stochastic fully connected random field

CNN treats each patch individually in the classification step, i.e., it does not apply spatial information. We incorporate the spatial information to refine the CNN's result by using a conditional random field. Research has shown the effectiveness of conventional conditional random field models in spatial structure modeling, however they use local connectivity which enforces undesired smoothness in boundaries [29, 1]. Long range connectivity and fully connected approaches address this problem [18]. Motivated by this fact, to this end we incorporate a stochastically fully connected conditional random field (SFCRF) to apply spatial information while preserving the boundaries.

SFCRFs are fully connected random fields in which cliques are defined stochastically [28]. SFCRF models the conditional distribution $P(Y|X)$ in the form of:

$$P(Y|X) = \frac{1}{Z(x)} \exp\Big(-\sum_i \psi_u(y_i, X) - \beta \sum_i \sum_{j \in C_i} \psi_p(y_i, y_j, X) \Big) \quad (1)$$

where Y is the ice concentration map given the corresponding SAR image X. $Z(X)$ is the partition function, ψ_u and ψ_p are the unary and pairwise potential function respectively. β plays the role of regularizer to determine the importance of the pairwise term (i.e., spatial information) in the model. C_i is the set of cliques for unit i which defines the connectivity of unit i with its neighboring units. This connectivity is defined by a stochastic function:

$$I(i,j) = \begin{cases} 1 & \text{if } \gamma P_{ij} Q_{ij} > u(0,1), \\ 0 & \text{if } \gamma P_{ij} Q_{ij} < u(0,1). \end{cases} \quad (2)$$

Where, P_{ij} measures the similarity between two nodes i and j, Q_{ij} measures the spatial closeness of these two nodes and γ encodes the sparsity of the connection. $u(0,1)$ is a random number drawn from an uniform distribution between 0 and 1. Closer and more similar nodes are more likely to be connected in the SFCRF. An illustration of SFCRF model is shown in Fig. 3. The clique connectives in the model are specified stochastically as (2), therefore, SFCRF is capable of modeling long range information efficiently while considering the computational complexity of the model.

The unary potential in (1) is formulated as:

$$\psi_u(y_i, X) = \exp(-\frac{(y_i - y_i^{(0)})^2}{2\sigma_u^2}) \quad (3)$$

where $y_i^{(0)}$ is the ice concentration calculated by CNN and σ_u controls the similarity measurement. The pairwise po-

tential is applied by enforcing the spatial similarity between two neighboring nodes regarding to their labels:

$$\psi_p(y_i, y_j, X) = \frac{(y_i - y_j)^2 P_{ij} Q_{ij}}{\sum_{j \in C_i} P_{ij} Q_{ij}} \quad (4)$$

in which, P_{ij} and Q_{ij} are weight that enforce the similarity and spatial closeness in to the pairwise potential. They are defined as:

$$P_{ij} = \exp\left(-\frac{\sum_k (x_{ik} - x_{jk})^2}{2\sigma_p^2}\right) \quad (5)$$

$$Q_{ij} = \exp\left(-\frac{(L_{ix} - L_{jx})^2 + (L_{iy} - L_{jy})^2}{2\sigma_q^2}\right). \quad (6)$$

To address the possible noise in the SAR image, the weights are computed in a patch based approach where k iterates through the patch around pixel i and j. The effect of weights P_{ij} and Q_{ij} are controlled by σ_p and σ_q respectively.

The final result of ice concentration map is computed by applying a maximum a posteriori (MAP) based on the conditional probability $P(Y|X)$. To find the best solution which maximizes the conditional probability, the energy function $\sum_i \psi_u(y_i, X) - \beta \sum_i \sum_{j \in C_i} \psi_p(y_i, y_j, X)$ is minimized. A gradient descent approach is used to optimize the energy function. Fig. 2 shows the effect of SFCRF at each iteration where the ice concentration input is refined by the proposed model.

3. Dataset

The dataset used to evaluate the proposed framework includes 15 dual-polarized (HH and HV) ScanSAR wide beam images of the Beaufort Sea acquired in 2010 and 2011, and their corresponding ice charts which are acquired from the Canadian Ice Service (CIS). Each scene covers a 500 km by 500 km area with 50 m by 50 m nominal pixel spacing. The SAR images are down sized by a factor of 1/8 (400 m nominal pixel spacing) to reduce the noise of the SAR images. The dates of the images are given in Table 1. The images span the melt season and freeze-up in the Beaufort Sea. A set of sample points generated from the ice charts are used as labels in the training data in this experiment. The effect of SFCRF on ice boundaries can not be evaluated using ice chart due to its coarse spatial resolution. Each pixel of the 15 scenes are, therefore, manually labeled to ice or water for the evaluation of ice/water classification results and the effectiveness of SFCRF. These labels are generated using a segmentation based scheme described in [8, 32] augmented with manual inspection.

4. Experiment and results

4.1. Training

The CNN is initialized by uniform random sampling between -0.05 and 0.05. The biases are initialized to 1 to improve learning speed of network using ReLU units. Mean square error is used as the cost function for training. Standard stochastic gradient descent (SGD) with weight decay 0.0005 and momentum 0.9 is used. Batch size is set to 128. An epoch training scheme [21] is adopted. Early stop is used to accelerate the training process [25]. 9 images are used for training, 3 images are used for testing and 3 are used for validation (Table 1). The CNN with the smallest validation error is adopted as the trained model.

The parameters of the SFCRF are evaluated and tuned on a set of image patches of dimension 128 by 128. The search window for potential connections is 101 by 101 so that the search area is big enough to find enough correct connections. The weight of the unary term is tuned to 0.4. The similarity of two pixels are calculated in the 3 by 3 windows around the two pixels. The SFCRF normally converges within 5 iterations on our test images.

The experiment is conducted on a computer equipped with one 8-core i7-2600 CPU, 32GB memory and one Nvidia GTX 780 graphic card. The training of CNN takes about 1 day using Pylearn2 [13]. The SFCRF is implemented in C++ and Matlab. Each iteration of the SFCRF on a image of size around 800 by 1000 takes less than 25 minutes.

4.2. Evaluation results

The achieved overall mean absolute differences between ice chart and the estimated ice concentration using CNN are 0.11, 0.12 and 0.11 for training, validating and testing dataset respectively. Selected results from training, testing and validation sets are shown in Fig. 5. The proposed method is able to generate ice concentration maps with well preserved boundaries for all the three sets. The ice water boundaries of the CNN output are in many cases in stronger agreement with the validation data when the SFCRF is used. As shown in Fig. 4, CNN overestimates the spatial extent of the ice-water boundary, which is corrected by SFCRF. It can also be observed in Fig. 6 that CNN-SFCRF is able to produce more finer ice concentration maps than that produced using CNN, which is coarser in nature.

The area under the ROC (receiver operating characteristic) curve and the classification accuracy are used to evaluate the classification results by simply thresholding on ice concentration estimates. Points on a ROC curve are pairs of false positive rate and true positive rate of the classification results obtained by using different thresholds on the refined ice concentration estimations. Details about generating ROC plots can be found in [10]. The accuracies are calculated using an ice concentration threshold of 0.4 which gives the highest overall accuracy. The performance evaluation is shown in Table 1. A consistent improvement in performance is brought by the use of SFCRF on CNN compared to the use of CNN only. The average classifica-

tion accuracy is 96.77% for validation data and 96.16% for testing data which is comparable to the results reported in [23].

Melting surface is a common cause of ice miss-classifications and under estimation of ice concentration. In Fig. 7, the dark regions are very likely to be melting ice at this time of year. Most of this region is correctly recognized by CNN. Details of ice concentration variations are captured by our proposed method while the ice chart indicates the whole image patch has an ice concentration being 0.6. In panels (d), (e) and (f), it is shown that the remaining misclassified areas using CNN output are mostly corrected by SFCRF. This suggests that the proposed method is robust to melting conditions. Ice concentration maps that contains more details than ice charts can be generated by the proposed method.

5. Conclusion

This work combines convolutional neural network and stochastic fully connected random field for the purpose of ice water concentration estimation from SAR images. We demonstrated the usefulness of ice charts as training data for ice water classification using CNN. In the present study the ice concentrations from the ice chart were mapped pixel-wise to the SAR image. The use of ice charts at a smaller scale than its original scale introduces representation errors in the training data, which potentially degrades the performance of the method. Using ice chart polygons as training data is one of our future research interests.

SFCRF is shown to improve boundaries between ice and water for most of the images considered. As part of our future investigations, we hypothesize that smaller scale structures may be better preserved if the connections found by SFCRF can be improved. This can be potentially be done using improved similarity metrics that better considers the image characteristics of SAR images, which will be our next step in the near future.

References

[1] R. Achanta, A. Shaji, K. Smith, A. Lucchi, P. Fua, and S. Susstrunk. Slic superpixels compared to state-of-the-art superpixel methods. *Pattern Analysis and Machine Intelligence, IEEE Transactions on*, 34(11):2274–2282, 2012. 3

[2] J. L. Awange and J. B. Kiema. Microwave Remote Sensing. In *Environmental Geoinformatics*, pages 133–144. Springer, 2013. 1

[3] Y. Bengio. Learning deep architectures for AI. *Foundations and trends in Machine Learning*, 2(1):1–127, 2009. 1

[4] M. Buehner, A. Caya, L. Pogson, T. Carrieres, and P. Pestieau. A new Environment Canada regional ice analysis system. *Atmosphere-Ocean*, 51(1):18–34, 2013. 1

[5] F. D. Carsey. *Microwave remote sensing of sea ice*, volume 68. American Geophysical Union, 1992. 2

[6] L.-C. Chen, G. Papandreou, I. Kokkinos, K. Murphy, and A. L. Yuille. Semantic image segmentation with deep convolutional nets and fully connected crfs. *arXiv preprint arXiv:1412.7062*, 2014. 2

[7] D. Ciresan and U. Meier. Flexible, high performance convolutional neural networks for image classification. *Proceedings Of The Twenty-second International Joint Conference On Artificial Intelligence*, pages 1237–1242, 2011. 2

[8] D. A. Clausi, A. K. Qin, M. S. Chowdhury, P. Yu, and P. Maillard. MAGIC : MAp-Guided Ice Classification System. *Canadian Journal of Remote Sensing*, 36:13–26, 2010. 4

[9] J. C. Curlander and R. N. McDonough. *Synthetic Aperture Radar*, volume 199. Wiley New York, 1991. 1

[10] T. Fawcett. Roc graphs: Notes and practical considerations for researchers. 2004. 4

[11] T. Geldsetzer, J. van der Sanden, and B. Brisco. Monitoring lake ice during spring melt using RADARSAT-2 SAR. *Canadian Journal of Remote Sensing*, 36(sup2):S391—-S400, 2010. 1

[12] R. S. Gill. SAR surface ice cover discrimination using distribution matching. In *Applications of SAR Polarimetry and Polarimetric Interferometry*, volume 529, page 55, 2003. 1

[13] I. J. Goodfellow, D. Warde-Farley, P. Lamblin, V. Dumoulin, M. Mirza, R. Pascanu, J. Bergstra, F. Bastien, and Y. Bengio. Pylearn2: a machine learning research library. *arXiv preprint arXiv:1308.4214*, 2013. 4

[14] O. M. Johannessen, V. Y. Alexandrov, V. Alexandrov, I. Y. Frolov, and L. P. Bobylev. *Remote sensing of sea ice in the Northern Sea Route*. Praxis Publishing Limited, 2007. 1

[15] A. Karpathy, G. Toderici, S. Shetty, T. Leung, R. Sukthankar, and L. Fei-Fei. Large-Scale Video Classification with Convolutional Neural Networks. *2014 IEEE Conference on Computer Vision and Pattern Recognition*, pages 1725–1732, June 2014. 2

[16] J. Karvonen, M. Simila, and M. Makynen. Open water detection from Baltic Sea ice Radarsat-1 SAR imagery. *Geoscience and Remote Sensing Letters, IEEE*, 2(3):275–279, 2005. 1

[17] J. A. Karvonen. Baltic sea ice SAR segmentation and classification using modified pulse-coupled neural networks. *Geoscience and Remote Sensing, IEEE Transactions on*, 42(7):1566–1574, 2004. 1

[18] P. Krähenbühl and V. Koltun. Efficient inference in fully connected crfs with gaussian edge potentials. In *Advances in Neural Information Processing Systems*, pages 109–117, 2011. 2, 3

[19] A. Krizhevsky, I. Sutskever, and G. E. Hinton. ImageNet classification with deep convolutional neural networks. In *Advances in neural information processing systems*, pages 1097–1105, 2012. 2

[20] Y. LeCun, L. Bottou, Y. Bengio, and P. Haffner. Gradient-based learning applied to document recognition. *Proceedings of the IEEE*, 86(11):2278–2324, 1998. 2

[21] Y. LeCun, L. Bottou, G. Orr, and K. Müller. Efficient backprop. In *Neural Networks: Tricks of the Trade*. 2012. 4

Table 1: Performance statistics

		Area_under_ROC_curve		Accuracy	
	Date	CNN	CNN-SFCRF	CNN	CNN-SFCRF
	20100730	0.9407	**0.9423**	0.8755	**0.8855**
	20100806	0.9612	**0.9652**	0.8985	**0.9032**
	20100822	**0.9862**	**0.9862**	**0.9508**	0.9466
	20100829	0.9827	**0.9770**	0.9405	**0.9459**
Train	20100909	0.9356	**0.9379**	**0.8966**	0.8952
	20100929	0.9916	**0.9924**	0.9815	**0.9822**
	20101003	0.9848	**0.9895**	0.9513	**0.9586**
	20101006	0.9956	**0.9967**	0.9738	**0.9771**
	20101008	**0.9951**	0.9943	**0.9946**	0.9945
	Average	0.9758	**0.9775**	0.9278	**0.9314**
Valid	20110709	**0.9970**	0.9967	0.9744	**0.9772**
	20110710	0.9886	**0.9925**	0.9659	**0.9722**
	20110720	**0.9890**	0.9873	**0.9596**	0.9595
	Average	0.9925	**0.9928**	0.9656	**0.9677**
Test	20110725	0.9927	**0.9937**	0.9706	**0.9721**
	20110811	0.9859	**0.9884**	0.9575	**0.9642**
	20110817	0.9834	**0.9876**	0.9409	**0.9493**
	Average	0.9885	**0.9910**	0.9557	**0.9616**

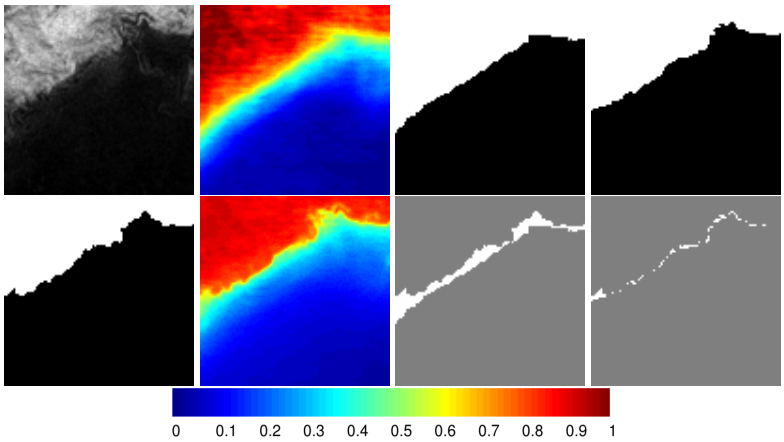

Figure 4: Boundary improvement. First row, from left to right: region extracted from HH band SAR image; ice concentration estimate using CNN; ice labels generated by CNN, ice labels generated by CNN-SFCRF. The second row from left to right: ground truth labels; ice concentration estimate using CNN-SFCRF; difference between CNN generated ice labels and ground truth; difference between CNN-SFCRF generated ice labels and ground truth. In all label images, white corresponds to ice and black corresponds to water.

[22] H. Lee, R. Grosse, R. Ranganath, and A. Y. Ng. Convolutional deep belief networks for scalable unsupervised learning of hierarchical representations. In *Proceedings of the 26th Annual International Conference on Machine Learning*, pages 609–616. ACM, 2009. 2

[23] S. Leigh and D. A. Clausi. Automated ice–water classification using dual polarization sar satellite imagery. *IEEE Transactions on Geoscience and Remote Sensing*, 52(9):5529–5539, Sept. 2014. 1, 5

[24] M. Lundhaug. ERS SAR studies of sea ice signatures in the Pechora sea and Kara sea region. *Canadian journal of remote sensing*, 28(2):114–127, 2002. 1

[25] L. Prechelt. Early stopping—but when? In *Neural Networks: Tricks of the Trade*, pages 53–67. Springer, 2012. 4

[26] B. Scheuchl, R. Caves, I. Cumming, and G. Staples. Automated sea ice classification using spaceborne polarimet-

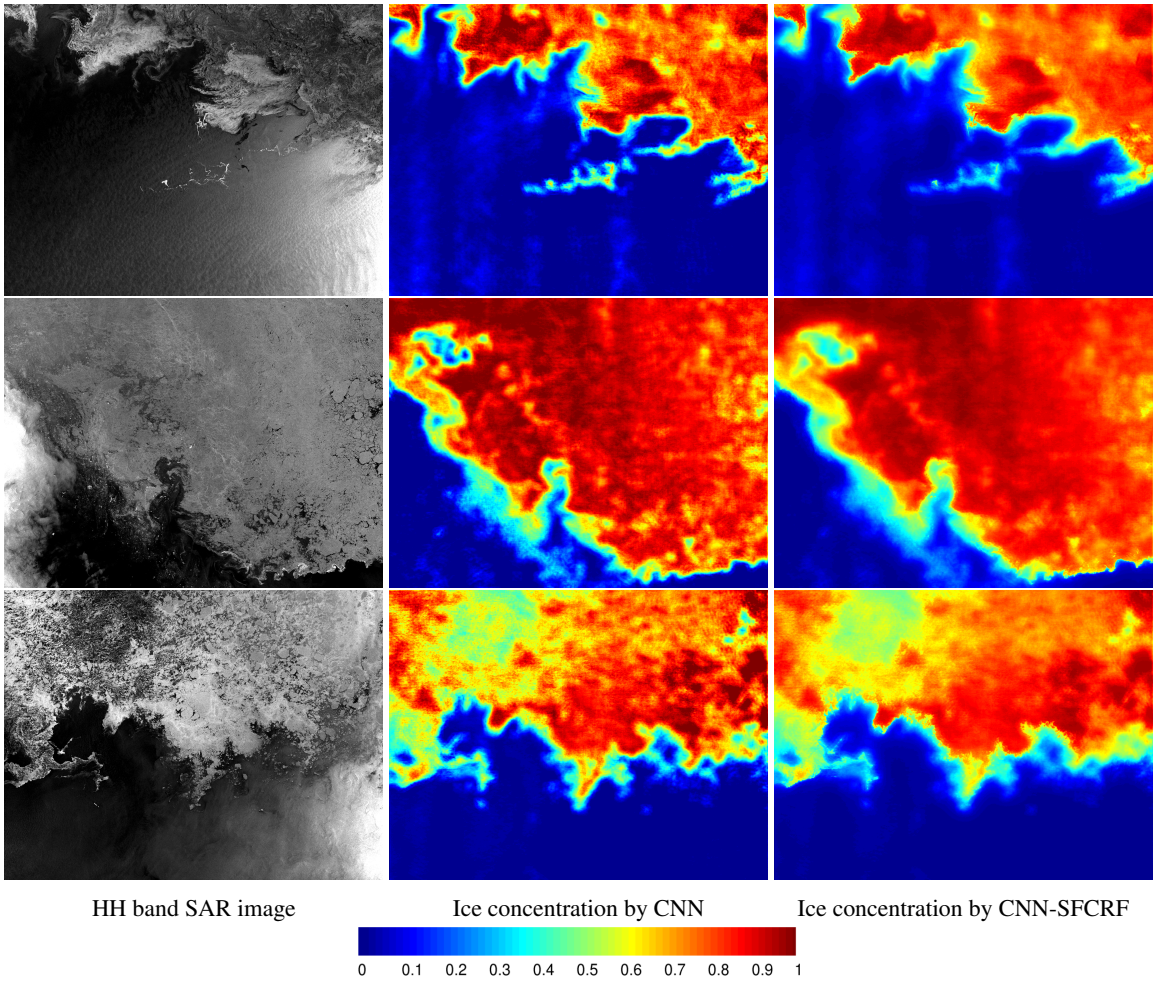

Figure 5: Results of scene 20101006 (first row), 20110720 (second row) and 20110811 (third row) from training, validating and testing dataset respectively. White corresponds to ice and black corresponds to water for label panels (second and third column). SAR images are enhanced for visualization.

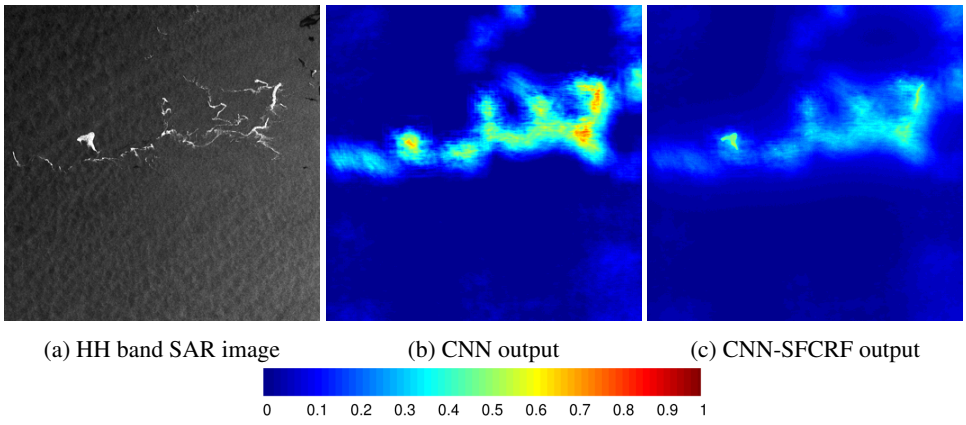

Figure 6: Example zoomed-in region of ice concentration maps generated using CNN and CNN-SFCRF in scene 20101006. Images are enhanced for visualization.

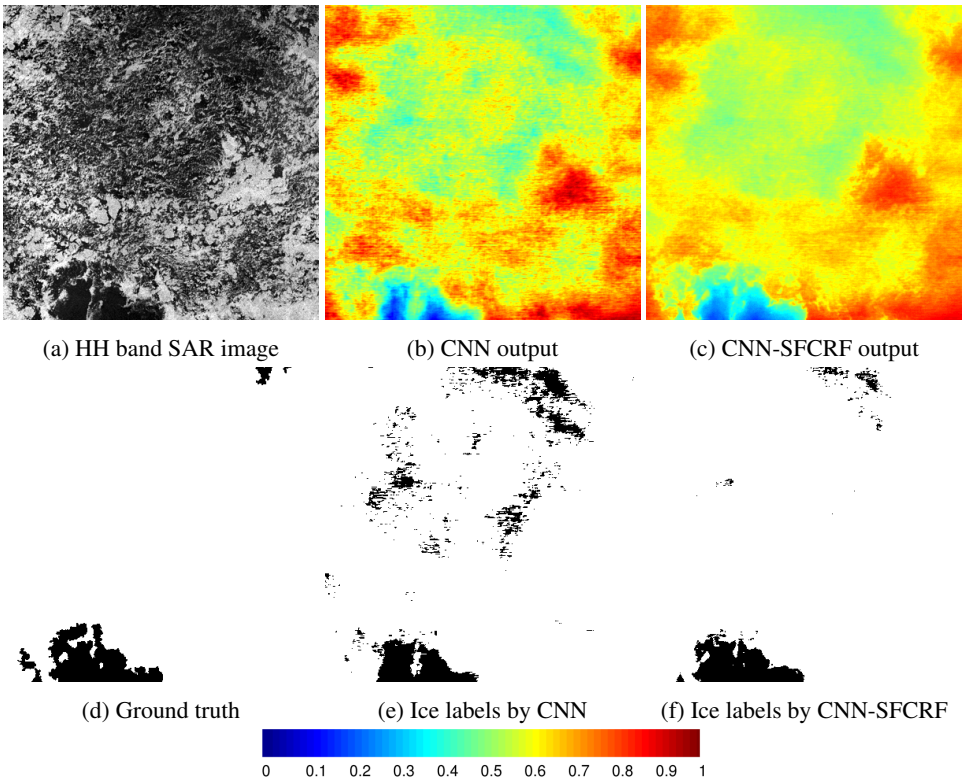

(a) HH band SAR image (b) CNN output (c) CNN-SFCRF output

(d) Ground truth (e) Ice labels by CNN (f) Ice labels by CNN-SFCRF

Figure 7: Example of correct ice concentration estimation and classification of melting ice from scene 20110811. Images are enhanced for visualization.

ric SAR data. In *Geoscience and Remote Sensing Symposium, 2001. IGARSS'01. IEEE 2001 International*, volume 7, pages 3117–3119. IEEE, 2001. 1

[27] B. Scheuchl, I. Hajnsek, and I. Cumming. Sea ice classification using multi-frequency polarimetric SAR data. In *Geoscience and Remote Sensing Symposium, 2002. IGARSS'02. 2002 IEEE International*, volume 3, pages 1914–1916. IEEE, 2002. 1

[28] M. J. Shafiee, A. Wong, P. Siva, and P. Fieguth. 2, 3

[29] J. Shotton, J. Winn, C. Rother, and A. Criminisi. Textonboost for image understanding: Multi-class object recognition and segmentation by jointly modeling texture, layout, and context. *International Journal of Computer Vision*, 81(1):2–23, 2009. 3

[30] L.-K. Soh, C. Tsatsoulis, D. Gineris, and C. Bertoia. ARKTOS: An intelligent system for SAR sea ice image classification. *Geoscience and Remote Sensing, IEEE Transactions on*, 42(1):229–248, 2004. 1

[31] D. N. Thomas and G. S. Dieckmann. *Sea ice*. Wiley-Blackwell, 2009. 1

[32] Q. Yu and D. A. Clausi. IRGS: image segmentation using edge penalties and region growing. *Pattern Analysis and Machine Intelligence, IEEE Transactions on*, 30(12):2126–2139, 2008. 4

[33] N. Y. Zakhvatkina, V. Y. Alexandrov, O. M. Johannessen, S. Sandven, and I. Y. Frolov. Classification of sea ice types in ENVISAT synthetic aperture radar images. *Geoscience and Remote Sensing, IEEE Transactions on*, 51(5):2587–2600, May 2013. 1